A combination of synchrotron and laboratory X-ray techniques for studying tissue-specific trace level metal distributions in *Daphnia magna*†

B. De Samber,[a] R. Evens,[b] K. De Schamphelaere,[b] G. Silversmit,[a] B. Masschaele,[c] T. Schoonjans,[a] B. Vekemans,[a] C. R. Janssen,[b] L. Van Hoorebeke,[c] I. Szalóki,[d] F. Vanhaecke,[a] G. Falkenberg[e] and L. Vincze*[a]

In the field of environmental toxicology, the study on the effects of the presence of transition metals such as Cu, Ni and Zn on the health of pelagic and benthic invertebrates is an important research topic. Fast dynamic 2D micro-XRF scanning and dynamic XRF micro-CT experiments on *D. magna*, a frequently used ecotoxicological model organism, allow the quantitative investigation of the accumulation of metals within specific organs with microscopic resolution. K-means clustering allows comparison of the concentrations of the elements of interest between different tissues/organs. Principal component analysis allows most of the significant statistical variations in these large and complex multivariate data sets to be explained. Also, by combining SR-XRF and absorption CT data sets using appropriate software packages, it becomes possible to unravel the tissue-specific 2D/3D distribution of metals *in-situ* within delicate organic samples on the 3–15 μm resolution level in an essentially non-destructive manner.

Introduction

Synchrotron radiation (SR) X-ray fluorescence (SR-XRF) microbeam techniques at second and third generation SR sources offer the potential of non-destructive multi-element analysis down to trace concentration levels with unrivalled spatial resolution among X-ray based analytical techniques. At these sources, relative detection limits at the sub-ppm (fg/ng) level can be achieved. With respect to absolute detection limits (DL), sub-micron sized X-ray beams can offer DLs below 10 ag for the most efficiently excited transition elements, with a potential lateral resolution level better than 100 nm.[1]

These characteristics of microbeam SR-XRF allow spatially resolved multi-element determination of major, minor and trace constituents in microscopic sub-volumes within biological specimens in an essentially non-destructive/non-invasive manner. However, the complexity of performing such an experiment is often quite considerable, involving dedicated sample preparation, transportation towards and experimenting in another environment, installing an appropriate experimental set-up and performing a thorough data analysis on large amounts of the spectral data.[2] In what follows, an illustrative example is given on the use of two- and three-dimensional (2D/3D) micro SR-XRF

methods in combination with other X-ray micro-imaging techniques in the field of environmental toxicology.

In the field of environmental toxicology, the study on the effects of the presence of transition metals such as Cu, Ni and Zn on the health of pelagic and benthic invertebrates is an important research topic. Efforts are being made to develop increasingly accurate biotic ligand models (BLMs),[3,4] which can then be used to predict the metal toxicity as a function of the metal concentration and the physicochemical characteristics of the surface water. On the basis of reliable BLMs, scientifically more relevant environmental regulations can be defined. For a further refinement and a more direct underpinning of these models, it is necessary to relate toxicological effects to tissue-specific and intracellular element distributions over the various internal organs of these organisms (for example respiratory/iono-regulatory tissues and digestive tissues). This also includes determining the relative contribution of different exposure routes (*i.e.* uptake *via* water or *via* the diet) to toxicological effects of metals.[5]

The freshwater crustacean *Daphnia magna* is a frequently used ecotoxicological model organism to investigate the mechanisms of toxicity of the metals mentioned above. Historically, it has often been difficult to link bioaccumulation to toxic effects in daphnids because total organism digestion (as needed for ICP-MS analysis for example) cannot distinguish the accumulation in critical tissues from whole body accumulation. The small size of these organisms (1 to 4 mm) does not allow a straightforward determination of the metal contents of tissues of interest by conventional techniques, such as dissection followed by acid digestion and subsequent analysis by atomic absorption spectrometry.[6] Moreover, transformation of delicate organic samples during the necessary extraction of the metal or species of interest from the sample and during the subsequent sample pre-treatment and separation process remains a frequently occurring problem.

aDepartment of Analytical Chemistry, Ghent University, Krijgslaan 281-S12, Ghent, B-9000, Belgium
bLaboratory of Environmental Toxicology and Aquatic Ecology, Ghent University, Jozef Plateaustraat 22, Ghent, B-9000, Belgium
cCentre for X-Ray Tomography, Department of Subatomic and Radiation Physics, Ghent University, Proeftuinstraat 86, Ghent, B-9000, Belgium
dInstitute of Experimental Physics, University of Debrecen, Bem tér 18/a, Debrecen, 4026, Hungary
eHamburger Synchrotronstrahlungslabor at DESY, Notkestr. 85, Hamburg, D-22603, Germany
† This paper is part of a JAAS themed issue on Synchrotron Radiation, with guest editors Alex von Bohlen and Metin Tolan.

Therefore, the ecotoxicological research on *D. magna* is ideal to illustrate recent trends in the field of 2D/3D scanning X-ray microfluorescence using synchrotron radiation, coupled with laboratory X-ray absorption tomographic techniques on biological systems. The *in-situ* analysis of the sample volume of interest with minimal damage caused by the X-ray microbeam allows the quantitative investigation of the accumulation of a wide range of metals within specific organs with microscopic resolution and offers an elegant solution to the previously stated problem. A variety of X-ray micro fluorescence scanning techniques is currently available, including (a) conventional µ-XRF scanning (2D), (b) µ-XRF computed tomography (2D/3D)[7] and (c) confocal µ-XRF imaging (2D/3D),[8] of which the first two are presented in this article. All these scanning modes can be used in a so-called "dynamic" mode, *i.e.* by moving the sample continuously through the microbeam with periodic data readout. On the one hand, this accelerates data collection, and in many cases reduces potential radiation damage of delicate biological specimens. One has to investigate thoroughly which scanning strategy to use in order to obtain the most valuable information during a given SR-experiment for a given analytical problem.

Also, advanced data processing procedures, such as K-means clustering algorithms, can be applied. This approach aims at segmenting the collected 2D/3D elemental data set into areas (clusters) with distinct elemental composition (representing the tissues/organs of interest), which can then be analyzed with more reliable statistics. In addition, the use of principal component analysis (PCA) allows most of the significant statistical variations in these large and complex multivariate data sets to be explained.[9]

As illustrated below, the use of complementary techniques such as laboratory X-ray absorption microtomography offers the possibility of an improved interpretation of the obtained micro-XRF data. It also aids the quantification of 2D/3D elemental imaging results by providing a full 3D tissue-density model, *i.e.* an accurate frame of reference for the very same sample which was investigated by scanning micro SR-XRF.[10,11] Three-dimensional absorption tomography allows the investigator to 'look inside' the sample without the need of dissection, and to overlay distributions of the elements of interest on the tissue structure in order to investigate elemental associations and biological structure–function relations.[12]

Experimental

Sample preparation

An important requirement during a synchrotron micro-XRF experiment is the conservation of the sample upon irradiation. Next to mechanical rigidity, this also implies that there should be no translocation of elements on a scale comparable with the resolution used during the micro-XRF scan. The pre-treatment of the *D. magna* (see Fig. 1a) poses additional challenges as compared to non-aquatic samples with low moisture content: their initially high water content makes them extremely delicate to handle, and drying may induce significant distortions of the sample structure including dislocation of elements on the microscopic level.
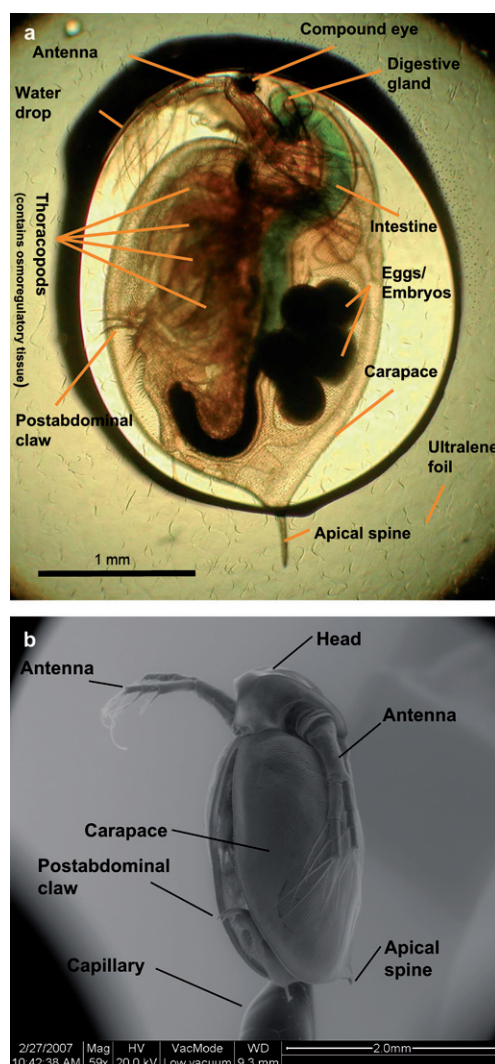

Fig. 1 (a) *Daphnia magna* in a drop of water on ultralene foil, seen through a transmission light microscope. (b) SEM analysis of the non-exposed HMDS-dried *D. magna* sample.

Cryofreezing of the sample during the analysis is a possible solution and was elegantly illustrated by Kanngießer *et al.*[13] by performing 2D confocal measurements on the root of common duckweed, kept frozen with a cold nitrogen gas stream. Nevertheless, the necessary facilities are often not available at synchrotron microspectroscopy beamlines. Moreover, unwanted effects, such as deposition of ice on the sample and mechanical vibration due to the applied cryostream can occur.

Critical point drying (CPD) works on more rigid samples, but applied to *D. magna*, it causes major shrinkage of the carapace in the region of the neck and the brood pouch during the analysis when using, *e.g.*, scanning electron microscopy (SEM), as previously reported by Laforsch and Tollrian.[14] The same authors used HMDS (1,1,1,3,3,3-hexamethyldisilazane) as drying agent in a successful preparation method for scanning electron microscopy (SEM) investigations of daphnids. The method is characterized by good preservation, low costs and easy operation without the requirement of special equipment. Considering these advantages, the *HMDS drying method* for

SEM analysis was adapted for the synchrotron micro-XRF analyses on daphnids by omitting the gold coating.

An adult *D. magna* for a first analysis was taken from the stock culture at the Laboratory of environmental toxicology, of which the details are described in ref. 15. The Zn concentration in the case of this culture is about 5–7 µg Zn L^{-1}, which is near-optimal for promoting Zn-dependent biochemical processes in *D. magna*. This sample is termed the "unexposed *D. magna*" in what follows.

In order to obtain insights into the possibility of determining tissue-specific element uptake and distribution following exposure to metal pollution, an adult *D. magna* was selected that was exposed for one week to 120 µg Zn L^{-1}, a concentration at which toxic effects started to appear in our earlier study.[15] The exposure was carried out in a test medium as described in ref. 15, with the exception that dissolved organic carbon was not added. This sample is further on termed the "exposed *D. magna*". It should be noted that, since the culture medium (corresponding to unexposed *D. magna*) and the test medium (corresponding to exposed *D. magna*) are not the same, definitive biological/physiological inferences should preferably not be made with respect to the differences in elemental distributions between these two samples, with the exception of differences in Zn contents and distributions.

Following the HMDS drying procedure described by Laforsch and Tollrian,[14] the *D. magna* samples were dehydrated in graded acetone solutions (70%, 80%, 90%, 2 × 98% and 2 × 100%) for 10 min each. Subsequently, the specimens were immersed in 1–1.5 mL HMDS (1,1,1,3,3,3-hexamethyldisilazane) in 20 mL glass vials. After 30 min, approximately 90% of the HMDS was removed and the vials were immediately transferred to a desiccator. The bottom of the desiccator was covered by silica gel beads and the desiccator itself was evacuated to avoid water contamination which would cause shrinkage in the specimens. The remaining HMDS was allowed to evaporate overnight under anhydrous conditions. After drying, the samples were inspected using an optical (reflection) microscope, and then glued onto the tip of a polymer support capillary, which in turn was fixed in a brass holder. The brass holder with the attached capillary and sample was subsequently inserted into a goniometer head which was mounted onto the rotation/scanning-stage of the synchrotron radiation micro-XRF set-up at Hasylab, Beamline L.

After SR-XRF analysis, the prepared samples were also visualised using scanning electron microscopy (SEM) (see Fig. 1b) (Quanta 200F from FEI). A low vacuum detection mode suitable for visualizing non-conducting samples without the need for applying conductive coating was used. As revealed by the SEM-images, in contrast with other sample preparation methods tested, the *D. magna* prepared using the above described HMDS drying procedure revealed an intact surface structure, proving the quality of this method. Since the samples showed no observable degradation as investigated by SEM and laboratory absorption microtomography after the SR-XRF measurements, we can conclude that the sample remained undamaged during the entire procedure.

Synchrotron radiation micro-XRF set-up

The scanning micro SR-XRF experiments were performed at Beamline L of the DORIS-III storage ring (4.465 GeV positron ring), HASYLAB (Hamburg, Germany). This beamline is dedicated to micro-XRF experiments using either white or monochromatic bending magnet excitation and mono- or polycapillary focusing, providing beam sizes of 5–20 µm.

The primary X-ray beam is generated by a 1.2 T bending magnet source, which provides a polychromatic spectral distribution with a critical energy of 16.6 keV. After initial low-energy filtering and collimation, the beam was monochromatized by a Ni/C multilayer monochromator at 20.7 keV.[16,17]

A single-bounce mono-capillary designed and manufactured at Cornell University[18] was used for focusing the monochromatic hard X-rays by means of total reflection. A micro-beamstop positioned in front of the base of the capillary blocks the part of the direct beam which would pass the capillary without reflection. This single-bounce ellipsoidal capillary produces a micro-beam of low divergence (< 4 mrad) when compared to polycapillaries and consequently, shows a larger working distance (~50 mm) and a higher energy cut-off for total reflection (> 25 keV). The lower divergence is necessary since µ-XRF-CT assumes a pencil beam along the beam path through the sample. The beam size at 20.7 keV incident energy was determined to be approximately 15 µm full width at half maximum (FWHM).[18] The SR-XRF spectra are measured under a 90° detection angle relative to the incident beam using a Radiant Vortex-EX silicon drift detector (SDD), having an active area of 50 mm^2 and a nominal crystal thickness of 350 µm. This energy-dispersive detector was coupled with a Canberra 2060 digital pulse processor and VME multichannel analyzer memory. A detector collimator of sufficient solid angle was used in order to detect the fluorescent radiation emerging from the full beam path within the sample during the micro XRF-tomography experiments. The emerging XRF signal is detected under an angle of 90° with respect to the incoming beam in order to reduce background contribution from Compton/Rayleigh scattering.

Next to optical sample visualisation and alignment using a long working distance microscope, the set-up makes it possible to perform micro-radiography using a high-resolution X-ray CCD camera (Photonic Science Coolview EM 1000, 1000 × 1000 pixels, 0.8 µm pixel size) under wide-beam illumination, *i.e.* when the single bounce capillary and micro beamstop are removed from the beam.[19,20] The latter CCD camera can be switched with an ionisation chamber in order to measure the micro beam intensity behind the sample under focused beam condition.

An additional ionisation chamber in front of the single bounce capillary measures the intensity of the incoming beam, which is used for normalization purposes and for deriving absorption data in combination with the transmitted signal measured by a second ionisation chamber behind the sample. Fig. 2a shows a side view of the experimental set-up, with the synchrotron radiation emerging from the right. Behind the sample, the above mentioned X-ray sensitive CCD camera is installed which allows high resolution radiography (1–2 µm). The sample stage comprises different motorised blocks for XYZ movement and rotation. Fig. 2b shows the top view of the experimental set-up: the monochromatized synchrotron radiation is focused by the single bounce mono-capillary, positioned on a hexapod (PI) stage. The produced microbeam illuminates the sample, which is mounted on a goniometer head attached to the XYZ scanning/rotation stage. [Fig 2c] shows a schematic overview of the set-up.
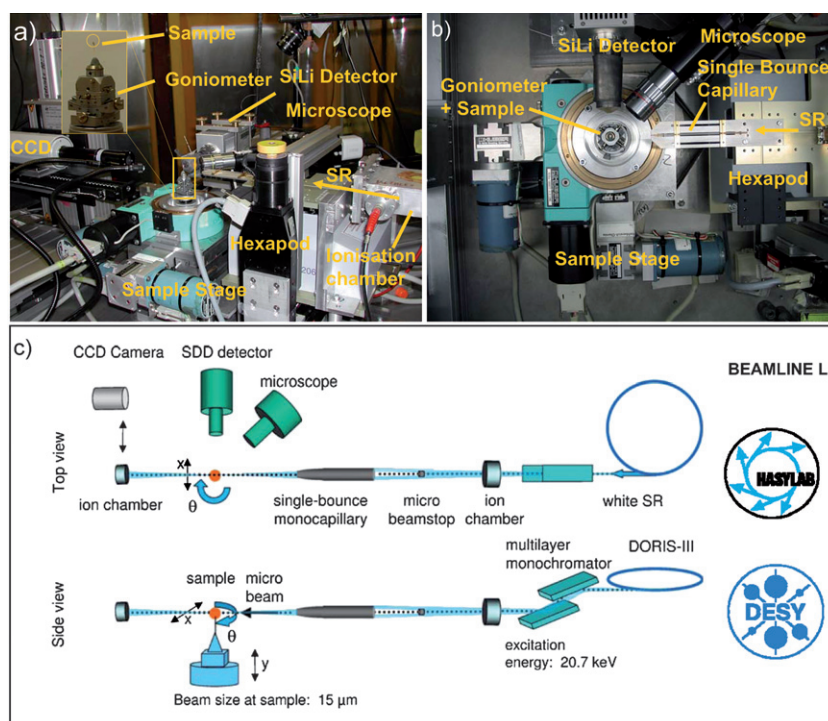
Fig. 2 (a) Top view of the experimental set-up at HASYLAB, Beamline L. (b) Side-view of the experimental set-up at HASYLAB, Beamline L. (c) Top view and side view (schematic) of the experimental set-up at HASYLAB, beamline L.

UGCT micro/nano CT set-up at Ghent University

The scanning micro SR-XRF experiments at Beamline L (HASYLAB) were complemented by absorption CT measurements at the UGCT micro/nano CT set-up at Ghent University, which was possible due to the excellent preservation of the samples during SR-XRF analysis.

The UGCT facility offers the possibility to investigate a wide variety of samples with sizes ranging from a few micrometers up to several centimeters. A cone shaped X-ray beam is delivered by a FXE-160.50 dual head transmission tube (160 kV, 900 nm focal spot size) from Feinfocus. Several hundreds of magnified radiographs of the sample are recorded by a Rad-Eye HR CMOS detector equipped with a Gadox scintillation screen (1200 × 1600 pixels). The projection data-set (typically 800 projections, 40 flat field images and 5 offset images) was reconstructed using the Octopus software.[21]

Results and discussion

Conventional 2D dynamic SR-XRF scanning

In order to obtain an organism-wide view on the tissue-specific elemental distribution and to investigate if 2D (conventional) micro SR-XRF scanning is appropriate to detect differences in Zn distribution between control and Zn-stressed organisms, it is necessary to scan the entire *D. magna*, of which the relevant areas are often as large as several square millimeters. Keeping the spatial resolution at 20 μm results in several 10 000 points per scan, requiring a (sub)-second measuring time per point in order to keep the duration of a scan within acceptable limits. Therefore, a so-called dynamic scanning mode was used, in which the

sample is moved continuously across the beam (instead of the stepwise motion corresponding to the conventional mode), with periodic readout of the XRF spectra from the data acquisition system. The multichannel analyser (MCA) integrates the spectra within a pre-defined time interval (sampling time) while the sample is being dynamically scanned. This provides a fast scanning capability in the sub-second per pixel regime with minimum time loss due to overhead.[22]

Both *D. magna* samples (exposed and unexposed) were positioned with their carapaces perpendicular to the incoming X-ray beam. This yielded a lateral view of the elemental distributions, which was considered the most informative view, given the bilateral symmetry of *D. magna*. Due to the light organic matrix (dry weight of the sample is approximately 100 μg), and the highly penetrating character of the applied 20.7 keV X-ray beam, all trace elements along the beam path within the *D. magna* are excited uniformly without considerable attenuation of the incident beam. Self-absorption effects for the induced fluorescence radiation can also be considered negligible for all but the lowest atomic number elements detected (*e.g.*, S, Cl, K).

The 2D dynamic scanning XRF maps from the unexposed (175 × 122 pixels) and exposed (175 × 142 pixels) *D. magna* were recorded using a step size of 20 μm and a data collection time of 0.3 s per pixel. These scans result in a total of 46 200 XRF spectra, representing several hundred MBytes of data. For both daphnids, a sum spectrum was generated first, which gives an overview of the (overall) detectable elemental composition of the entire organism. The sum spectrum of both samples, normalised to the Compton scattering signal in order to account for differences in illuminated mass, is shown in Fig. 3. Note that the
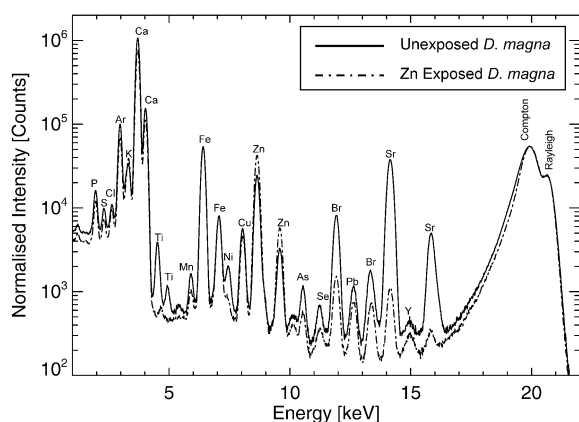
Fig. 3 Sum spectra of the exposed and unexposed *D. magna*, normalised to the Compton signal.

Compton scattered peak of the unexposed *D. magna* shows a greater distortion towards lower energies than the exposed *D. magna*. Since the sample alignment for both samples was identical, this could be due to slightly different beam properties in the second run or a slight difference in density between both samples. As expected, one can immediately observe that the Zn-exposed *D. magna* exhibits a higher total Zn content than the unexposed specimen, which was previously observed by Zn-determination on the basis of total organism digestion followed by AAS analysis (ref. 15). It can be clearly seen that the exposed *D. magna* appears to contain lower amounts of Br and Sr, however it is not clear if this difference is linked with the elevated Zn exposure or caused by differences in Br and Sr concentrations in the culture *vs.* exposure medium. Additional experiments, in which daphnids are exposed to a range of Zn concentrations in a test medium with the same Br and Sr concentrations, are needed to resolve this uncertainty.

Some unexpected elements, such as Y, Ti and Pb are also present in the sum spectra. As shown below, individual analysis of the sum spectra of the areas of interest within *D. magna* reveals that the Ti was present in the glue on the support capillary and not within the *D. magna*. The Pb signal is probably originating from scattering/fluorescence effects from beamline components, whereas the Y signal is due to fluorescent radiation originating from the Y-containing YAG crystal, present in the CCD camera positioned near the sample.

The sum spectra were used to identify the elements (P, S, Cl, Ar, K, Ca, Mn, Fe, Ni, Cu, Zn, Se, Br, Rb, Sr and Pb) which needed to be included in the fitting-model of the spectrum evaluation software AXIL.[23] The software package MICROXRF2[23] was used to generate the elemental maps based on a recursive fitting procedure of the individual point spectra. All elemental maps were normalised to a live time (LT) of 1 s and a DORIS-III current of 100 mA and were corrected for detector dead time in order to be able to quantify the data and make comparisons between the elemental maps possible.

In order to quantify the XRF measurements, a carefully determined amount of NIST SRM 1577 (Bovine Liver) powder was pressed to a pellet of 13 mm internal diameter resulting in an areal density of 19.7 mg cm^{-2}. A line scan of 25 measuring points with individual live time of 200 s was performed in order to verify the homogeneity of the obtained pressed pellet.[24] The homogeneity of the reference material was within statistical uncertainty (3–5%) for Ca, Fe and Zn. Based on the obtained sum spectrum from the line scan on the standard (see Fig. 4a) and using the certified concentration values, the absolute and relative detection limits and elemental yield curve were calculated as shown in Fig 4b. All values were corrected for self absorption effects within the thin SRM pellet. Absolute detection limits for the elements of interest are in the femtogram range. These values correspond to relative detection limits in the 0.01–0.10 µg g^{-1} for the most efficiently excited/detected elements assuming a beam size of 15 µm (FWHM), which was available during our experiments at Beamline L. The same experimental conditions were used for the measurements on the analysed *D. magna* samples.

By using the elemental yield curve shown in Fig. 4b, an estimation of the areal concentrations of the elements Zn, Fe and Ca of both *D. magna* was performed by dividing the normalised element intensities within the XRF-maps with the elemental yields. Although no self-absorption correction is applied, this first order approximation can be considered adequate to obtain semi-quantitative results for direct comparison between the
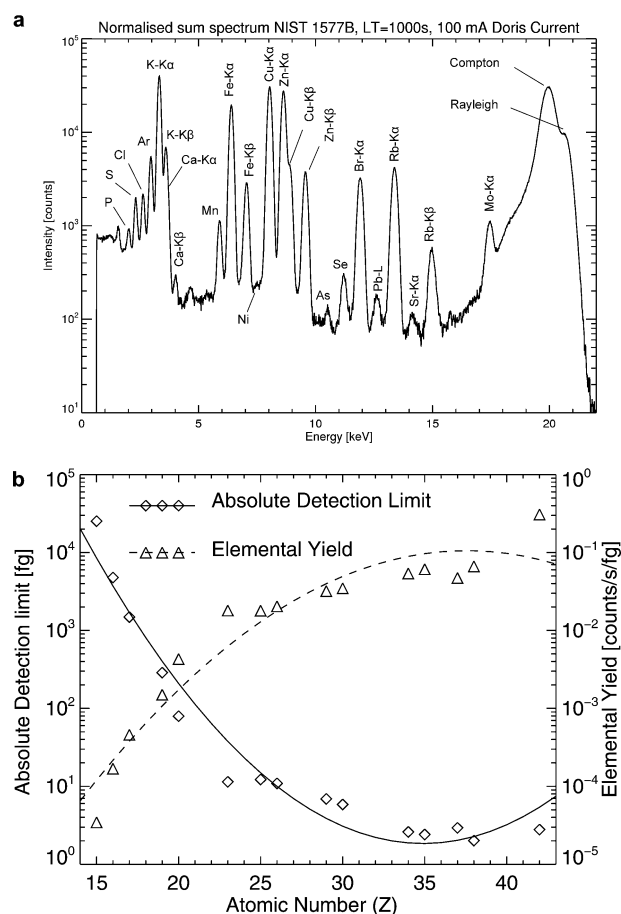

Fig. 4 (a) NIST SRM 1577 (Bovine liver) sum spectrum (pellet with an areal density of 19.7 mg cm^{-2}). The monochromatic incident X-ray beam had an energy of 20.7 keV. (b) Typical absolute detection limits using a live time of 1000 s derived from SRM NIST 1577 (Bovine Liver) using the micro-XRF set-up installed at HASYLAB Beamline L.

exposed and unexposed case. The calculated critical areal density values below, in which so-called thin-sample (linear) models can be applied for the considered elements (Ca, Fe, Zn) in a biological matrix excited by 20.7 keV photons (matrix composition is approximated by C) is well above the maximum values obtained in the element map (e.g., 0.041 g cm^{-2} for Ca; 0.215 g cm^{-2} for Fe). The calculated areal concentration maps for Ca, Fe and Zn in this first order approximation for both D. magna samples are shown in Fig. 5.

When comparing the Zn distribution of the non-exposed and the exposed daphnid, a distinct enrichment of Zn can be observed in (A) the gill-like osmoregulatory tissue, (B) the gut and (C) the digestive gland (Fig. 1a). The latter two are part of the digestive system of D. magna and are involved in nutrient absorption as well as the holocrine secretion of digestive enzymes.[25] The accumulation in gills may suggest that zinc accumulation may interfere with osmoregulation, as in fish.[26] The accumulation in the digestive system may suggest that nutrient assimilation from food is a possible target of Zn toxicity. It has indeed recently been shown that gene expression related to digestive processes in D. magna was altered following Zn exposure.[27] Alternatively, Zn accumulation in the digestive gland could also be the result of a detoxification strategy, whereby secretory vesicles are used to eliminate metals from the body, a process which is commonly observed in mussels.[28] However,

Fig. 5 Two-dimensional micro-XRF elemental maps (Zn, Fe and Ca) for the unexposed and exposed D. magna.

having obtained these data, some questions still remain unsolved. First, using only the 2D μ-XRF data, it remains unclear whether elevated levels of Zn in the gut region are located in the gut or in the gut epithelium. In order to answer this question, virtual cross-sections need to be obtained using μ-XRF computed tomography (or confocal μ-XRF) to get a better insight in the internal structure and elemental distribution of the sample. Second, there is a need to analyse the average elemental concentrations of different substructures of interest within these elemental maps based on K-means clustering. Third, the metal accumulations should be correlated with the different tissue structures which can be visualized using absorption μ-CT.

The evaluation of μ-XRF images results in data sets that are multidimensional: intensity values for the elements included in the AXIL model are calculated from the spectra recorded at the positions of the image map. An elegant way to study the properties of such multidimensional data sets is to apply multivariate analysis methods. E.g., PCA may help to eliminate data redundancies and to extract relevant information from the overwhelming amount of data. It is an analysis technique well known for its ability to remove collinearity and to reduce the dimensionality of data sets. In this way, PCA helps to interpret the data by the determination of which elements contribute to the principal components, and to help to classify the pixel data on the basis of their elemental properties. Using the new set of principal components, one can depict variables (elements) and objects (pixels) with similar or different characteristics. Combining element specific loading plots with their corresponding pixel specific score plots, one needs to investigate only a very few graphs, very often these are the most important principal components. A full description of this data reduction method and its application on XRF data sets has been published elsewhere.[9] In addition to PCA, grouping of objects (pixels) can be done by means of dedicated clustering strategies. In this work, the K-means clustering method is successfully applied to group pixels that provide equal (or similar) compositional information.[9] The additional advantage of this approach is that the resulting sum spectra corresponding to groups of pixels with similar composition feature (much) lower noise levels than the individual pixel spectra. In this work, the combination of PCA and the K-means clustering method has been applied as a powerful exploration tool to understand and to summarize the structure of the D. magna data sets as will be shown in the following.

Fig. 6 shows the K-means clustering of the unexposed D. magna data set when requesting 10 clusters using the Ca, Fe and the Compton information, since using these signals, the clusters were best coinciding with the different tissue structures/organs of interest. Note that before the actual clustering a square-root data pre-treatment is necessary in order to compensate for the Poisson counting statistics and a normalisation is performed in order to give equal weight to each element. Next to the air (CLR1) and clusters constituting the paraffin/support capillary (CLR3, CLR9, CLR10), we observe the brood pouch (CLR2), the gut (CLR4), the front exoskeleton (CLR5), the antennae (CLR6), the gill tissue (CLR7), and the eggs/eye (CLR8). From PCA on the clustering data, i.e. based on the elemental intensities calculated from the cluster sum spectra, as shown in Fig. 7 where the score (a) and loading (b) plots are
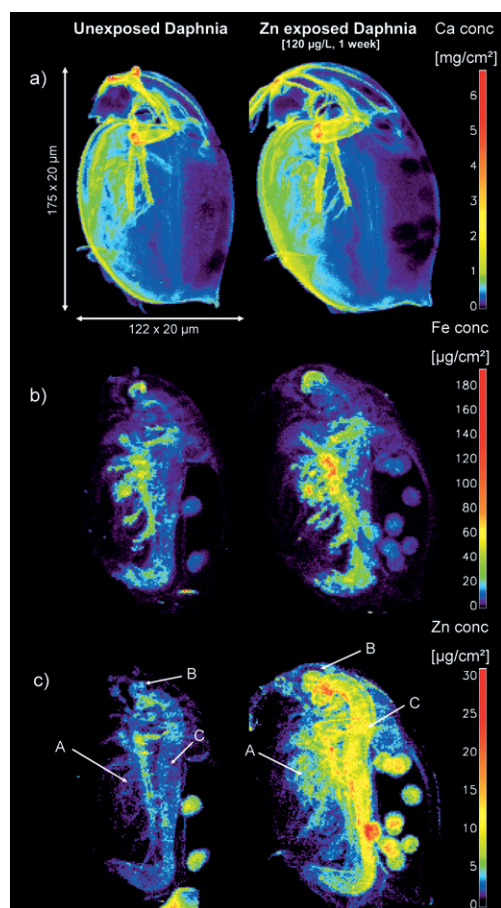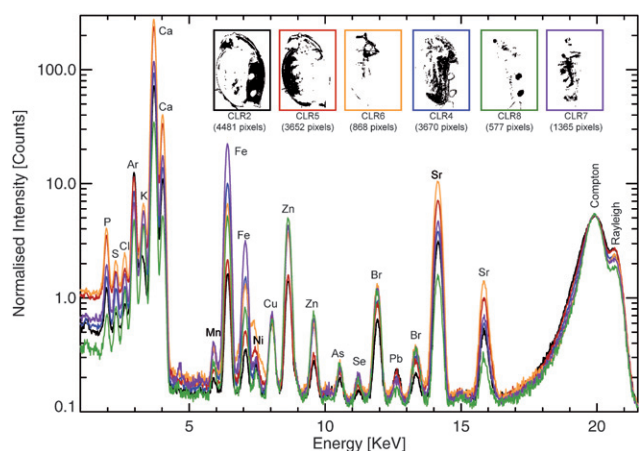
Fig. 6 K-means clustering results obtained from the unexposed *D. magna*. CLR2 (black): brood pouch, CLR5 (red): front exoskeleton, CLR6 (orange): antennae, CLR4 (blue): gut, CLR8 (green): eggs/eye, CLR7 (purple): gill tissue.
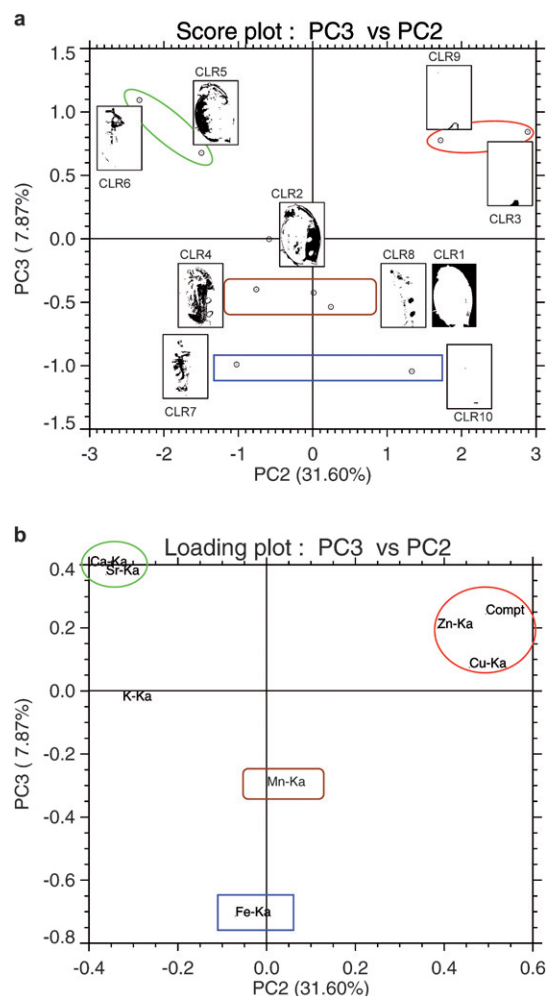

Fig. 7 a) Results from PCA analysis on the unexposed *D. magna*: score plot. CLR6: antennae, CLR5: front exoskeleton, CLR9: surface capillary + glue, CLR3: bulk capillary + glue, CLR4: gut, CLR8: eggs/eye, CLR1: air, CLR10: tip support capillary, CLR2: brood pouch. (b) Results from PCA analysis on the unexposed *D. magna*: loading plot.

presented for the most significant combination of the 2nd and 3rd most important component, we can immediately notice a correlation between Ca and Sr, but also between Zn, Cu and the Compton scattering signal. We also see that Fe does not correlate with any of the other elements, although a (minor) correlation with Mn seems possible. This strengthens the assumption that an efficient clustering is obtained by using only the Ca, Fe and Compton information as mentioned above. By association with the corresponding score biplot, we can also easily relate the antennae (CLR6) and the front exoskeleton (CLR5) with Ca/Sr, the gill tissue (CLR7) and the tip of the capillary (CLR 10) and to a lesser extent the gut (CLR4) and eggs/eye (CLR8) with Fe, the capillary tip (CLR9 + 10) and eggs/eye with Zn.

The corresponding sum spectra of the different clusters obtained are shown in Fig. 6. In order to compare the presence of elements in the different clusters, all sum spectra were normalised to the average density of CLR7 by using the Compton scattering signal. From these results, it can be concluded that the different tissues indeed show different metal enrichments. For instance, the antennae (CLR 6) and the front exoskeleton (CLR 5) have a higher Ca and Sr concentration than other tissues. The occurrence of high amounts of Ca in the exoskeleton is often reported for crustaceans as well as other animals with a calcified exoskeleton. In the carapax of *Daphnia*, Ca is suggested to be mainly associated with carbonate and phosphate minerals, which renders it a rigid structure as protection against predators.[29,30] The gill tissue (CLR7) has the highest Fe concentration of all tissues. The enrichment of Fe in the gill tissue is most likely related to the gill's respiratory function and, hence, to the presence of haemoglobin which is the most important oxygen transport molecule in *Daphnia*.[31,32] The Zn content is highest in eggs/eye (CLR8), although differences with the antennae (CLR6), gill (CLR7) and gut (CLR 4) are less pronounced. Note that the Ti signal in these clusters completely disappeared, since the Ti contamination is not present in the clusters of interest. Also note that valuable information is obtained regarding the elemental content of clusters from which the element maps were too noisy, *e.g.*, for Mn, As, Se.

By applying a similar K-means clustering procedure on the exposed *D. magna*, it is also possible to isolate the structures of interest such as the gut, gill tissue and eggs/eye for the exposed *D. magna*. In Fig. 8 the Compton normalised sum spectra of the structures of interest are compared between both samples. For clarity, only the energy range for the elements Mn up to Sr was selected. Br, Sr, As, Se and Pb are present to a higher extent in the unexposed *D. magna*, but it is unclear if this is due to differences in the Zn concentration in the water or due to other differences between culture and exposure medium. It is, however, more interesting to focus on the comparison between the Zn contents and tissue distribution of non-exposed vs. exposed *D. magna*. First, no increased Zn accumulation is observed in the eggs of the exposed *Daphnia*, which may suggest that Zn transfer from mother to offspring is tightly regulated. Furthermore, the proportional increase of tissue-specific Zn accumulation after Zn exposure is the highest in gut tissue, followed by a smaller difference in the gill tissue. The higher Zn accumulation in the digestive tract after Zn exposure, compared to the gills, is interesting because this tissue is only subjected to an indirect Zn
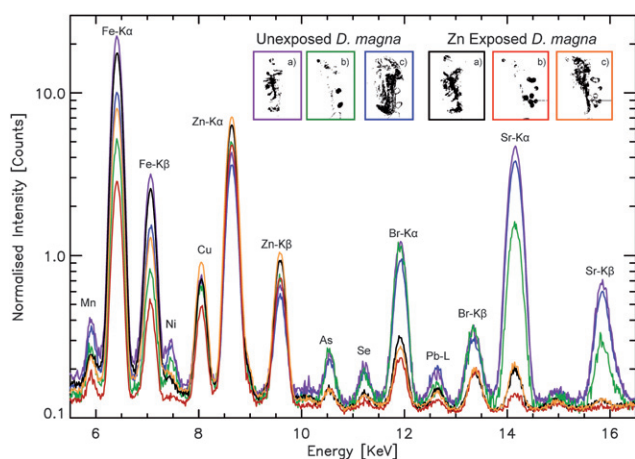
This journal is © The Royal Society of Chemistry 2008

J. Anal. At. Spectrom., 2008, **23**, 829–839 | 835

Fig. 8 Results from K-means clustering: comparison between the unexposed and exposed *D. magna*. (a) Gill tissue, (b) eggs/eye, (c) gut.

Fig. 9 Scaled Ca-Kα, Zn-Kα and Fe-Kα elemental maps, each assigned to a single color channel, red, green and blue respectively (left). RGB composed image, containing the combined information of the previous three images (right).

exposure, after ingestion of algal food that has become contaminated by Zn from the water. The occurrence of high Zn amounts in the gut epithelium and/or lumen could have an influence on the production and secretion of digestive enzymes,[27] and/or on the biochemical activity of these enzymes themselves.[33] Thus, impaired nutrient assimilation could be a toxicological target of Zn exposure. The accumulation of Zn in the gill tissue can disturb osmoregulatory processes[26] and impair the influx of Ca^{2+}, which in turn can lead to hypocalcaemia.[34] Further work, *e.g.* whereby Zn accumulation and physiological effects are investigated simultaneously for a range of different Zn concentrations, is needed to establish causal links between tissue specific Zn accumulation and disturbance of physiological processes.

A very illustrative way to visualize the simultaneous/complementary presence of elements can be obtained by creating composite images of the elements lying the furthest away from each other in the most significant score plot, *e.g.* in this case of the non-exposed *D. magna*. The element distribution of Ca, Zn and Fe were scaled from 0 to 255 and assigned the colours red, green and blue respectively, so that each colour channel in a pixel (red, green, blue) is assigned to a specific element and the brightness of the colour in a pixel is scaled to the concentration. An RGB image can then be created by overlaying these 3 coloured element maps, revealing the different elemental distributions at one glance with an indication of correlating or complementary behaviour of the elements in question. For example, from the data shown in Fig. 9, it can be deduced that the carapace is rich in Ca, the eggs and gut in Zn and the osmoregulatory tissue in Fe. This confirms the data obtained with the clustering analysis (see above and Fig. 6).

Dynamic XRF computed tomography

As mentioned earlier, conventional 2D micro XRF (dynamic) scanning elemental maps provide no depth information of the sample. In order to gain insight in the elemental distribution within a given cross section through the sample, X-ray fluorescence computed tomography (XRF-CT) was used. The technique can be easily performed on a regular scanning micro XRF set-up with the addition of a sample rotation stage to the
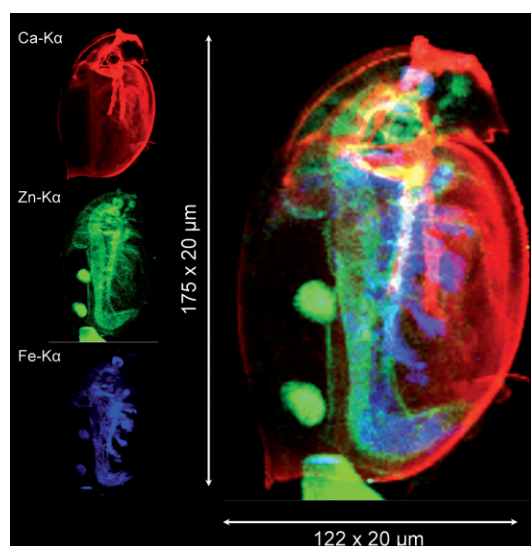
usual *x–y* linear stages. By performing repeated linear scans at a fixed sample-height under a large number of observation angles (*i.e.* taking different views of the sample) around a given sample axis and recording the emerging fluorescent and scattered signals, the conventional X-ray fluorescent mapping is replaced by a micro XRF-CT experiment. In this way, one obtains a special representation of the elemental intensity distributions across the investigated cross-section of the sample, called elemental sinograms. The usual 2D elemental distribution in the investigated horizontal sample plane (*i.e.* the tomographic plane perpendicular to the vertical rotation axis) is obtained by a mathematical reconstruction procedure called filtered backprojection algorithm.[7] Also here, a continuous scanning mode for the horizontal line scans was used in order to shorten the measuring time.

Fig. 10 shows XRF microtomography results taken from the unexposed *D. magna*. The recorded sinograms (see Fig. 10, left column and upper right) correspond to 165/156 (unexposed/exposed *D. magna*) translation steps of 20 μm and 180 rotation steps of 2°, with a live time of 1.3/1.0s (exposed/unexposed), through the region of the gut, gill tissue and eggs. By using the single bounce capillary and the CCD camera without the micro beamstop, it was possible to accurately track the position of the microbeam on the tissue of interest. This technique was used in order to determine the right height at which the μ-XRF-CT maps are made. The reconstruction of the tomographic data sets displayed was done *via* a filtered backprojection algorithm, without using self-absorption corrections. Self-absorption effects cannot be observed due to the low density matrix of the organic material, even for low energy lines such as Ca-Kα ($E_{Kα} = 3.69$ keV). Several methods exist to correct for the attenuation of both primary and fluorescent X-rays within the sample matrix, but the use of these algorithms is beyond the scope of this article. Fig. 10 illustrates elemental distributions of Ca, Zn and Fe within given cross-sections of the unexposed *Daphnia* (middle column and lower right side). These distributions agree with the previously
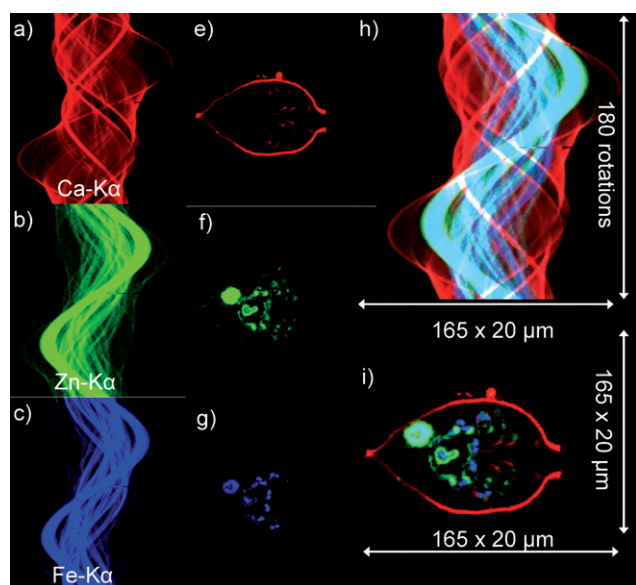
Fig. 10 Scaled Ca-Kα, Zn-Kα and Fe-Kα elemental sinograms, each assigned to a single color channel, red, green and blue respectively (left). RGB composed sinogram and CT RGB composed reconstruction, containing the combined (reconstructed) information of the previous three images (right).

measured conventional 2D μ-XRF scanning results: a Ca-rich exoskeleton, Zn enrichment in eggs and gut and Fe enrichment in the osmoregulatory tissue (epipodites). The Zn cross-sectional data also clearly show that the Zn concentration in the gut epithelium of the non-exposed *Daphnia* is higher than the concentration in the gut lumen, an observation that could not be made using conventional 2D μ-XRF (projection) maps. It would be instructive to apply the same computed tomography technique to the Zn-exposed *Daphnia* to determine whether the Zn enrichment detected in the gut region (as observed in Fig. 5 and 8) is actually due to accumulation in gut epithelial tissue or whether it is due to Zn that is present in the gut lumen. Fig. 10 also confirms the lower concentration of Ca in the back of the carapax as compared to the front part, which was already concluded from the cluster sum spectra (Fig. 6).

As shown earlier by the loading plots of the PCA analysis, the 2D elemental distributions of Ca and Sr are closely correlated, as expected. A basic way to explore such elemental correlations in greater detail is to plot the X-ray intensity pertaining to one element against the intensity obtained for another throughout the series of pixels that constitute the image. In case two elements follow the same distribution throughout the sample, a linear correlation becomes visible in such correlation plots. However, even in case of homogeneous samples, self-absorption effects of the fluorescent radiation in the sample causes these correlation graphs to differ significantly from straight lines.[35] In this aspect, a comparison between the correlation plot of the 2D elemental distributions and the CT results for Ca and Sr provide us with a valuable tool to verify to which extent the absorption effects are present. Fig. 11 illustrates such a scatter plot of the square root of the Ca-Kα intensity (in order to correct for the Poisson counting statistics) *versus* the square root of the Sr-Kα intensity for the 2D elemental distributions and the CT elemental distribution. One
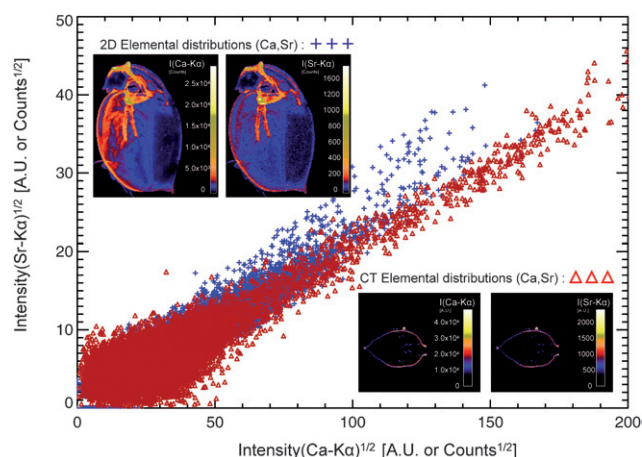

Fig. 11 Scatter plot of the square root of the Ca-Kα intensity *versus* the square root of the Sr-Kα intensity for the 2D elemental distributions (blue cross) and the CT elemental distributions (red triangles) for the unexposed *D. magna*.

can observe a similar slope for both curves, although a slightly higher slope for the 2D element distributions occurs at higher count rates, indicating only a minor presence of self absorption effects for the Ca-Kα lines, thus strengthening the hypothesis that a first order approximation for quantifying the element maps (Fig. 5) is justified.

Combined SR micro-XRF and laboratory absorption micro-CT

As previously mentioned, the conventional 2D micro-XRF (see Fig. 9) and micro-XRF CT data (see Fig. 10) visualising *e.g.* the accumulation of various metals should be ideally correlated with the different tissue structures of *D. Magna* with high accuracy.

In the example below, a 3D absorption micro-CT image of the unexposed *D. magna* was rendered using VGSTUDIOMAX,[36] of which images with a resolution of 3 μm are given in Fig. 12a–b. The different internal organs such as intestine, gill tissue, eggs, compound eye and muscle fibers are clearly visible. Unlike SEM, the complete 3D morphology of the sample can be investigated, revealing not only a good surface quality in our case, but also an excellent preservation of the internal structure as a result of the preparation method[14] at a higher resolution level than used for the micro SR-XRF analyses. It can also be noted that after micro
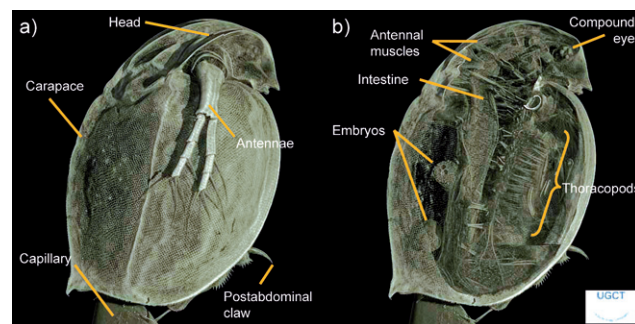

Fig. 12 (a) Three-dimensional absorption micro-CT: rendered surface image of *D. magna*. (b) Three-dimensional absorption micro-CT: rendered inner structure of *D. magna*.
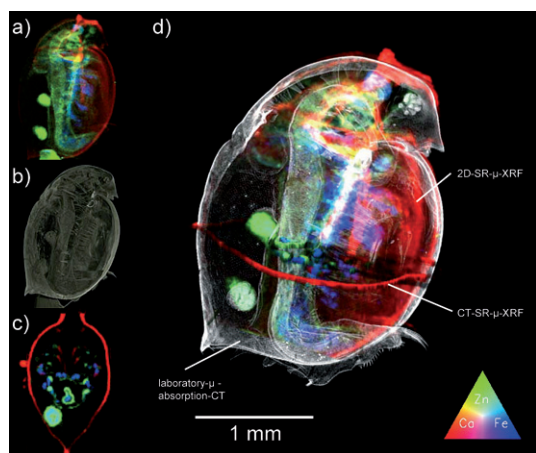
This journal is © The Royal Society of Chemistry 2008

J. Anal. At. Spectrom., 2008, **23**, 829–839 | 837

Fig. 13 (a) RGB composed image of the scaled 2D Ca, Zn, Fe elemental distributions of the unexposed *D. magna*. (b) 3D absorption micro-CT rendering of the inner structure of *D. magna*. (c) RGB composed image of the scaled Ca, Zn, Fe elemental cross sections within the unexposed *D. magna*. (d) 3D rendered image of the unexposed *D. magna*, combining laboratory absorption micro-CT and synchrotron 2D/CT micro-XRF data.

SR-XRF and SEM analysis, the surface of the sample was still intact.

By using the software package VGSTUDIOMAX, it was possible to combine the micro-XRF tomography results from given slices and the absorption micro-CT data in a single dataset, illustrated in Fig. 13, using typical reference markers (*e.g.*, support capillary, sample boundaries). The white dataset gives a full 3D absorption reconstruction of the daphnid (3 μm resolution) obtained *via* the UGCT micro/nano CT set-up at Ghent University. Two RGB composed μ-XRF datasets obtained at Hasylab, Beamline L are also incorporated in the image: a 2D μ-XRF dynamic scan (width: 175×20 μm, height: 122×20 μm) and a micro-XRF computed tomography scan (width: 165×20 μm, height: 165×20 μm) through the gill tissue, eggs and gut. The colors red, green and blue are the scaled Ca, Zn and Fe intensities, proportional to the elemental concentrations (note that the capillary was removed from the combined image for clarity). This image thus contains not only 3D density/absorption coefficient information on the 3 μm level, but also elemental concentration information for several metals, in 2D projection and CT modes, spatially resolved on the 15 μm scale.

Conclusions and outlook

In this article, different synchrotron radiation based scanning X-ray micro-fluorescence techniques were applied in an eco-toxicological case study. Emphasis was put on the importance of a suitable sample preparation technique for biological material when using X-ray microbeam techniques.

Different scanning micro-XRF techniques were applied on *D. magna*, which proved to be a valuable alternative for other (destructive) techniques. Fast dynamic 2D micro-XRF scanning allows a quick overview of the elemental distributions (Ca, Fe, Zn) over the whole organism on a 15 μm spatially resolved level. The *in-situ* analysis of the sample volume of interest with

a minimal influence of the X-ray microbeam allowed the quantitative investigation of the accumulation of metals within specific organs with microsopic resolution.

Performing K-means clustering on the obtained 2D datasets allowed the measured complex elemental distributions to be segmented, thus providing statistically more reliable cluster-spectra from sub-regions of interest, and subsequently allows comparison of the concentrations of the elements of interest (*e.g.* Zn) between different tissues/organs within a single organism, but also between differently exposed *D. magnas*. The use of PCA analysis makes it possible to group the clusters (representing tissues/organs of interest) according to their elemental concentrations present and to reveal elemental associations/correlations.

Dynamic XRF micro-CT allowed a more detailed analysis of the internal distribution of elements in a single slice without the need of cutting/damaging the sample. A better insight in the accumulation of certain metals within given organs/tissue layers was obtained.

The combination of X-ray absorption micro-CT was used to generate a full 3D model on a resolution level of 3 μm, providing density information on the sample. By this density matrix, the internal structure/morphology of the sample is revealed. The various organs within the daphnids can clearly be recognised and the preservation of the internal structure owing to the preparation technique can be verified. X-ray absorption micro-tomography offers the possibility to facilitate the interpretation and aid the quantification for 2D/3D elemental imaging results. By combining both SR-XRF and absorption CT data sets using appropriate software packages, it becomes possible to unravel the tissue-specific 2D/3D distribution of metals *in-situ* within delicate organic samples in an essentially non-destructive manner. The illustrated example demonstrates the potential of combining ecotoxicological experiments with techniques which can both visualize and determine the elemental composition of biological samples on the microscopic scale.

In a next phase of this research, emphasis will be placed on analysing *D. magna* samples that have been exposed to Zn *via* water, *via* the diet and *via* a combination of both. Except for Zn, concentrations of all other elements in the water will be kept constant in order to be able to make sound conclusions about (i) the relative importance of and interaction between different exposure routes with respect to tissue specific accumulation of Zn and (ii) about the influence of Zn exposure on the internal distribution of other elements (*e.g.*, Ca, Sr, Cu, Fe) Furthermore, these spatially resolved measurements will be complementary to a stable isotopic tracer experiment already performed by ICP-MS on *D. magna*.[6]

Acknowledgements

References

1 C. Schroer, O. Kurapova, J. Patommel, J. Feldkamp, B. Lengeler, M. Burghammer, C. Riekel, L. Vincze, A. van der Hart and M. Küchler, *Appl. Phys. Lett.*, 2005, **87**, 124103.

2 B. Vekemans, K. Janssens, L. Vincze, F. Adams and P. Vanespen, *X-Ray Spectrom.*, 1994, **23**, 278–285.

3 P. Paquin, J. Gorsuch, S. Apte, G. Batley, K. Bowles, P. Campbell, C. Delos, D. Di Toro, R. Dwyer, F. Galvez, R. Gensemer, G. Goss, C. Hogstrand, C. Janssen, J. MCGeert, R. Naddy, R. Playle, R. Santore, U. Schneider, W. Stubblefield, C. Wood and K. Wu, *Comp. Biochem. Physiol. C: Pharmacol. Toxicol.*, 2002, **133**, 3–35.

4 D. Heijerick, K. De Schamphelaere and C. Janssen, *Environ. Toxicol. Chem.*, 2002, **21**, 1309–1315.

5 K. De Schamphelaere, M. Canli, V. Van Lierde, I. Forrez, F. Vanhaecke and C. Janssen, *Aquat. Toxicol.*, 2004, **70**, 233–244.

6 L. Balcaen, K. De Schamphelaere, C. Janssen, L. Moens and F. Vanhaecke, *Anal. Bioanal. Chem.*, 2008, **390**, 555–569.

7 L. Vincze, *Developments in X-ray tomography IV*, in *X-ray Fluorescence Microtomography and Polycapillary based Confocal Imaging using Synchrotron Radiation*, ed. U. Bonse, SPIE-Bellingham, Washington, 2004.

8 L. Vincze, B. Vekemans, F. Brenker, G. Falkenberg, K. Rickers, A. Somogyi, M. Kersten and F. Adams, *Anal. Chem.*, 2004, **76**, 6786–6791.

9 B. Vekemans, L. Vincze, F. E. Brenker and F. Adams, *J. Anal. At. Spectrom.*, 2004, **19**, 1302–1308.

10 B. Golosio, A. Somogyi, A. Simionovice, P. Bleuet and J. Susini, *Appl. Phys. Lett.*, 2004, **84**, 1–3.

11 B. Golosio, A. Simionovici and A. Somogyi, *J. Appl. Phys.*, 2003, **94**, 145–150.

12 S. A. Kim, T. Punshon, A. Lanzirotti, L. Liangtao, J. M. Alonso, J. R. Ecker, J. Kaplan and M. L. Guerinot, *Science*, 2006, **314**, 1295–1298.

13 B. Kanngießer, W. Malzer, M. Pagels, L. Lühl and G. Weseloh, *Anal. Bioanal. Chem.*, 2007, **389**, 1171–1176.

14 C. Laforsch and R. Tollrian, *Arch. Hydrobiol.*, 2000, **149**, 587–596.

15 B. Muyssen, K. De Schamphelaere and C. Jansen, *Aquat. Toxicol.*, 2006, **77**, 393–401.

16 K. Peeters, K. De Wael, L. Vincze and A. Adriaens, *Anal. Chem.*, 2005, **77**, 5512–5519.

17 G. Falkenberg, O. Claus and T. Tschentscher, *Hasylab Annu. Rep.*, 2001, **1**, 1–9.

18 G. Falkenberg, K. Rickers, D. Bilderback and R. Huang, *Hasylab Annu. Rep.*, 2003, **1**, 1–4.

19 Photonic Science, Coolview EM 1000/TV, Electron Multiplication Low Light Level CCD Camera with Digital Gain Management System, Operating Manual.

20 B. De Samber, G. Falkenberg and L. Vincze, *Hasylab Annu. Rep.*, 2006, **1**, 1389–1390.

21 Octopus, Scanner independant CT reconstruction software for fan beam, cone beam and parallel beam geometry, www.xraylab.com.

22 G. Falkenberg, T. Kracht and M. Küchbacher, *Hasylab Annu. Rep.*, 2005, **1**, 91–95.

23 B. Vekemans, K. Janssens, L. Vincze, F. Adams and P. Van Espen, *Spectrochim. Acta, Part B*, 1995, **50**, 149–169.

24 L. Kempenaers, C. De Koster, W. Van Borm and K. Janssens, *Fresenius' J. Anal. Chem.*, 2000, **369**, 733–737.

25 T. Schultz and J. Kennedy, *Tissue Cell*, 1976, **8**, 479–490.

26 C. Hogstrand, P. M. Verbost, S. E. W. Bonga and C. M. Wood, *Am. J. Phys.*, 1996, **270**, 1141–1147.

27 H. C. Poynton, J. R. Varshavsky, B. Chang, G. Cavigiolio, S. Chan, P. S. Holman, A. Loguinov, D. Bauer, K. Komachi, E. Theil, E. J. Theil, E. J. Perkins, O. Hughes and C. D. Vulpe, *Environ. Sci. Technol.*, 2007, **41**, 1044–1050.

28 I. Marigómez, M. Soto, M. Cajaraville, E. Angulo and L. Giamberini, *Microsc. Res. Tech.*, 2002, **56**, 358–392.

29 N. Alstad, L. Skardal and D. Hessen, *Limnol. Oceanogr.*, 1999, **44**, 2011–2017.

30 S. WÆrvagen, N. Rukke and D. Hessen, *Freshwater Biol.*, 2002, **47**, 1866–1878.

31 R. Pirow, F. Wollinger and R. Paul, *J. Exp. Biol.*, 1999, **202**, 553–562.

32 R. Pirow, F. Wollinger and R. Paul, *J. Exp. Biol.*, 1999, **202**, 3089–3099.

33 Z. Chen, L. Mayer, D. Weston, M. Bock and P. Jumars, *Environ. Toxicol. Chem.*, 2002, **21**, 1243–1248.

34 D. Spry and C. Wood, *Can. J. Fish. Aquat. Sci.*, 1985, **42**, 1332–1341.

35 A. Somogyi, K. Janssens, L. Vincze, B. Vekemans, A. Rindby and F. Adams, *Spectrochim. Acta, Part B*, 2000, **55**, 75–89.

36 VGSTUDIOMAX, www.volumegraphics.com.